J. Fluid Mech. (2011), *vol.* 679, *pp.* 288–314.
doi:10.1017/jfm.2011.137

Dynamic roughness model for large-eddy simulation of turbulent flow over multiscale, fractal-like rough surfaces

W. ANDERSON AND C. MENEVEAU†

Department of Mechanical Engineering and Center for Environmental and Applied Fluid Mechanics, the Johns Hopkins University, 3400 North Charles Street, Baltimore, MD 21218, USA

(Received 31 August 2010; revised 24 January 2011; accepted 14 March 2011; first published online 3 May 2011)

Many flows especially in geophysics involve turbulent boundary layers forming over rough surfaces with multiscale height distribution. Such surfaces pose special challenges for large-eddy simulation (LES) when the filter scale is such that only part of the roughness elements of the surface can be resolved. Here we consider LES of flows over rough surfaces with power-law height spectra $E_h(k) \sim k^{\beta_s}$ $(-3 \leqslant \beta_s < -1)$, as often encountered in natural terrains. The surface is decomposed into resolved and subgrid-scale height contributions. The effects of the unresolved small-scale height fluctuations are modelled using a local equilibrium wall model (log-law or Monin–Obukhov similarity), but the required hydrodynamic roughness length must be specified. It is expressed as the product of the subgrid-scale root-mean-square of the height distribution and an unknown dimensionless quantity, α, the roughness parameter. Instead of specifying this parameter in an *ad hoc* empirical fashion, a dynamic methodology is proposed based on test-filtering the surface forces and requiring that the total drag force be independent of filter scale or resolution. This dynamic surface roughness (DSR) model is inspired by the Germano identity traditionally used to determine model parameters for closing subgrid-scale stresses in the bulk of a turbulent flow. A series of LES of fully developed flow over rough surfaces are performed, with surfaces built using random-phase Fourier modes with prescribed power-law spectra. Results show that the DSR model yields well-defined, rapidly converging, values of α. Effects of spatial resolution and spectral slopes are investigated. The accuracy of the DSR model is tested by showing that predicted mean velocity profiles are approximately independent of resolution for the dynamically computed values of α, whereas resolution-dependent results are obtained when using other, incorrect, α values. Also, strong dependence of α on β_s is found, where α ranges from $\alpha \sim 0.1$ for $\beta_s = -1.2$ to $\alpha \sim 10^{-5}$ for $\beta_s = -3$.

Key words: turbulence modelling, turbulence simulation, turbulent boundary layers

1. Introduction

Due to their prevalence in geophysics and engineering, turbulent boundary layer flows over rough surfaces have received sustained attention over many decades. The research topic was reviewed recently by Jiménez (2004) and Castro (2007). Since the early works by Schlichting (1936) and Nikuradse (1950), in the engineering literature

† Email address for correspondence: meneveau@jhu.edu

the focus has been on estimating the velocity shift, ΔU, in the logarithmic profile in response to surface roughness. In experiments, surface roughness has often been achieved with sand grains, leading to the concept of equivalent sand-grain roughness height k_s. In geophysical flows, the logarithmic profile is commonly expressed in terms of an effective roughness height z_0 (the Monin–Obukhov similarity theory, Monin & Obukhov 1954). In general, streamwise velocity profiles obtained from laboratory or field experiments, or direct numerical simulations (DNS) of rough wall-bounded flows, can be used *a posteriori* to deduce such hydrodynamic roughness length scales.

Much attention has been focused on surfaces with roughness elements that can be described by one or a few characteristic length scales, such as cubes, spherical or ellipsoidal bumps, or sinusoidal shapes. Many recent studies have yielded relevant experimental and computational data. For instance, Cheng & Castro (2002) and Castro, Cheng & Reynolds (2006) present wind-tunnel experimental results for flow over an urban-like staggered array of blocks. Coceal *et al.* (2006) use DNS to simulate similar roughness element configurations, finding close agreement. Orlandi & Leonardi (2006) and later Orlandi & Leonardi (2008) use DNS to study flows over surfaces with various types of roughness elements, created with combinations of wedges (at different orientations), cubes and cylinders. Also, Bhaganagar, Kim & Coleman (2004) and Bhaganagar (2008) use the immersed boundary method within DNS to model flow over three-dimensional (3D) ellipsoidal 'egg carton' roughness elements. In their work, the height amplitude of the roughness elements is varied to study the corresponding hydrodynamic response. Colebrook & White (1937) investigated transitionally rough pipe flows with surfaces containing two sizes of sand grains. More recently, Schultz & Flack (2005) extend the work of Colebrook & White (1937) in the fully rough regime. For recent experimental data on flow over rough surfaces in pipes, channels and developing boundary layers, see Shockling, Allen & Smits (2006), Allen *et al.* (2007), Bakken *et al.* (2005) and Schultz & Flack (2007).

Nakayama, Hori & Street (2004) use DNS to study flow over surfaces composed of two sinusoids in the streamwise direction, where the wavelength and amplitude of the second wave is much smaller than the first. The flow field is then spatially filtered with filter width sufficient to simultaneously remove details of the second surface wave. For comparison, the spatially filtered large-eddy simulation (LES) equations are then solved for flow over this smoothed surface. Differences between the LES and DNS data are used by Nakayama *et al.* (2004) to develop additional terms in the filtered (LES) momentum equation to account for pressure and skin-friction drag from the unresolved, subgrid-scale (SGS), wavy surface.

Effective roughness lengths have been deduced from a variety of field experimental data sets in atmospheric flows. In Raupach, Antonia & Rajagopalan (1991), a detailed review of rough-wall boundary-layer flows is presented, including estimates of z_0 for flow over various types of plant canopies (these were compiled from earlier works by Garratt 1977 and Jarvis, James & Landsberg 1976). Raupach (1994) presents a simple model for roughness length z_0 and displacement height d estimation based on existing non-hydrodynamic information such as the canopy height and frontal area index. Shaw & Schumann (1992) use LES to study atmospheric boundary layer (ABL) flows over a deciduous forest canopy, where local pressure drag forces from the canopy are imposed with a canopy stress model.

Brown, Hobson & Wood (2001) perform LES of neutrally buoyant ABL flow over rolling hills with homogeneous roughness distribution and compare the numerical results with wind-tunnel results; later, in a related work, Allen & Brown (2002) investigated flow over topographic features similar to those considered in Brown

et al. (2001), but in which the height of the 'ridges' changes sufficiently to induce flow separation. A number of studies have also focused on spatially heterogeneous distributions of roughness. For instance, Avissar & Pielke (1989) develop parameterizations for the SGS influence of surface heterogeneity in mesoscale numerical simulations. Other studies on such spatially heterogeneous roughness distributions include Hobson, Wood & Brown (1999), Bou-Zeid, Meneveau & Parlange (2004) and Bou-Zeid, Parlange & Meneveau (2007). Chow & Street (2009) use the advanced regional prediction system (ARPS) LES code for simulations of flow over a hill.

As reviewed above, most prior efforts have been devoted to surfaces with roughness characterized by a single or few length scales. The geometric form of many natural surfaces is multiscale and fractal-like, such as evolved fluvial landscapes (Rodriguez-Iturbe *et al.* 1994), the wind-driven ocean surface and tree canopies. In recent years, there has been growing interest in interactions of turbulence with objects characterized by a wide hierarchy of length scales. Examples include the studies of properties of turbulence decaying in the wake downstream of fractal objects (Queiros-Conde & Vassilicos 2001; Staicu *et al.* 2003; Hurst & Vassilicos 2007; Seoud & Vassilicos 2007), and numerical simulations of fractal tree-like shapes in high-Reynolds-number boundary layers (Chester & Meneveau 2007; Chester, Meneveau & Parlange 2007).

In this paper, we address the question of modelling flow over surfaces described by a height field $h(x, y)$ that displays a very broad range of length scales and features (x and y correspond to the streamwise and transverse directions in simulation of the mean flow, respectively), a problem that has received little attention by the community. Specifically, LES of flow over multiscale surfaces when roughness elements span scales in a range that includes both resolvable and unresolved scales. That is to say, applications without the existence of a clearly defined 'scale separation'. Natural fluvial landscapes temporally evolve through erosive processes leading to fractal-like branching geometries (Rodriguez-Iturbe *et al.* 1994; Rodriguez-Iturbe & Rinaldo 1997). Numerically, one can generate a fluvial landscape surface by solution of a modified version of the Kardar–Parisi–Zhang (KPZ) equation. Starting with a surface that features a dominant gradient with an additional field of low-amplitude white noise superimposed, and letting erosive forces dynamically change the surface based on simple rules, a network of channels will evolve. Evolved fluvial landscapes display scale-similarity over a broad range of length scales, and accordingly can be described by power laws, typically with a -2 spectral slope (Passalacqua *et al.* 2006). The tremendous range of length scales present in fluvial landscapes presents special challenges for numerical investigations, just as it does in turbulent flows at common (engineering and environmental) Reynolds numbers.

Synthetic multiscale fractal-like surfaces can also be generated conveniently by cumulative superposition of random-phase Fourier modes (RFM), whose amplitudes vary with wavenumber (based on pre-defined spectral exponent) to ensure that the final surface exhibits prescribed power-law spectra. Such synthetic surfaces are attractive for systematic studies focusing on the effect of spectral exponent on the characterization of roughness, and identification of landscape statistics that may be useful for estimation of hydrodynamic length-scale parameterizations (such as the root-mean-square, r.m.s., of the height distribution). Figure 1(a) shows a sample RFM surface of this kind with spectral exponent $\beta_s = -2$. In this work, we will consider rough surfaces characterized by power-law height spectra with various exponents (in some cases, to be statistically similar to natural examples).

The essence of LES relies on spatial filtering of flow field variables and subsequent parameterization of dynamically important information removed during filtering. In

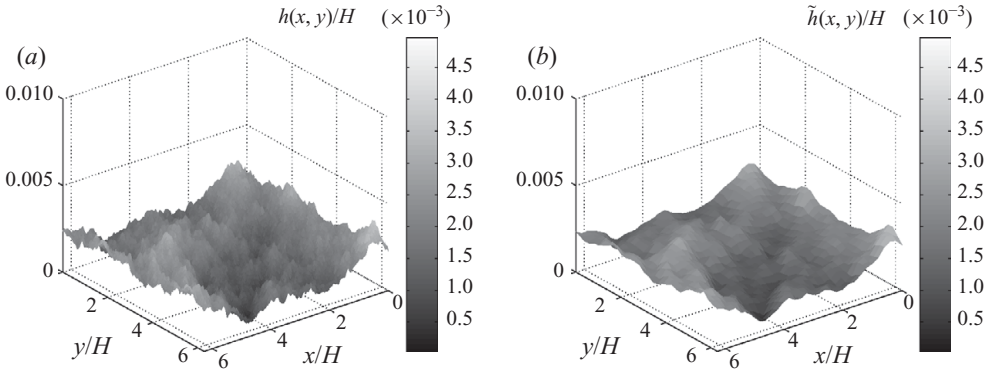

FIGURE 1. Multiscale landscape built with random-phase Fourier modes and representative spectral exponent $\beta_s = -2$: (*a*) unfiltered surface on a 1024×1024 grid-point resolution and (*b*) filtered surface on 32×32 resolution.

the case of surfaces with wide ranges of scales, this process imposes a spatial filtering operation on the bounding surface. For example, in the case of LES of ABL flows, the rough terrain could be composed of spatial length scales ranging from kilometres down to millimetres, and the flow scales range from the meteorologic mesoscale to (diffusive) length scales. The LES filter width, Δ, may be of the order of 10–50 m, i.e. falling in between the relevant range of scales for *both* the terrain and the turbulent flow in the ABL. We propose a formulation based on decomposing the surface height distribution $h(x, y) = \tilde{h}(x, y) + h^{SGS}(x, y)$ into a resolved filtered height $\tilde{h}(x, y)$ and the difference, the subgrid or subfilter height distribution, $h^{SGS}(x, y)$, containing the smaller-scale height fluctuations. Filtering is denoted by a $\widetilde{(\ldots)}$ and is understood to be a spatial (two-dimensional, 2D) filter at length scale Δ comparable to the scale used to filter the LES fields (velocity, pressure, etc.) in the bulk of the flow. Figure 1(*b*) shows the RFM sample surface (figure 1*a*), filtered at a scale $\Delta = L/N = 2\pi H/N$ for $N = 32$.

It is reasonable to assume that the effects of the resolved height distribution $\tilde{h}(x, y)$ can be treated with existing numerical methods, such as terrain-following (body-fitted) coordinate systems (Gal-Chen & Sommerville 1975*a*,*b*; Wan & Porté-Agel 2010), the immersed boundary method (Iaccarino & Verzicco 2003; Mittal & Iaccarino 2005) or unstructured meshes for turbulent flows interacting with complex geometry (Mavriplis 1997). In this work, horizontally resolved variations in height will be represented using the surface-gradient-based drag (SGD) model, described in Anderson & Meneveau (2010). The SGD model is a variant of the immersed boundary method based on an imposed body force proportional to the local gradient of the surface that is normal to the local flow. The focus of this paper is on the development of a dynamic physics-based model for the high-pass-filtered range of landscape wavenumbers (i.e. $h^{SGS}(x, y)$), instead of using empirical models that may not adequately represent the landscape effects in LES.

When all roughness elements are unresolved, the classical approach is to model roughness effects by using a hydrodynamic roughness scale in the context of the logarithmic law for rough boundary layers. At high Reynolds numbers when viscous drag on roughness elements can be neglected (fully rough), the concept of equivalent sand-grain roughness height k_s arises in the expression $U(z)/u_* = \kappa^{-1} \ln(z/k_s) + B^*$, where $U(z)$ is the mean streamwise velocity at height z, u_* is the friction velocity, κ is the von Kármán constant, k_s is an effective roughness, and $B^* \approx 8.5$. In geophysical

contexts, the equivalent expression $U/u_* = \kappa^{-1}\ln(z/z_0)$ is often used, both relations being connected through $z_0 = k_s \exp(-B^*\kappa)$. It is generally possible *a posteriori* to deduce an equivalent roughness length from measured or simulated velocity profiles. However, as stressed in Schultz & Flack (2009), to use only geometric properties of the surface height distribution to predict *a priori* an equivalent roughness length remains an open problem of significant challenge and importance.

Various formulations have been proposed. Perhaps the most straightforward is to express the hydrodynamic roughness length in terms of the r.m.s. of the height fluctuations. In experiments of turbulent pipe flow where the amplitude of roughness heights followed an approximately Gaussian distribution, Zagarola & Smits (1998) report the relation $k_s = 3\sigma_h$, and thus $z_0 \approx 0.1\sigma_h$ for $\kappa \approx 0.4$ and $B^* = 8.5$. Extensive experiments on flow over pyramidally shaped roughness elements by Schultz & Flack (2009) show that the characteristic slope of the surface can affect the results, up to a critical value above which the slope becomes irrelevant. Very recently, Flack & Schultz (2010) use an extensive compilation of experimental data for flows in the fully rough regime over surfaces with various types of roughness elements. They use the data to identify which surface geometry moments are most relevant as scaling parameters, and find that σ_h and skewness of the surface height probability distribution function, s_k, display strongest correlation with the experimentally recorded values of k_s. An empirical relation is presented:

$$k_s \approx 4.43\sigma_h\,(1 + s_k)^{1.37}\,. \tag{1.1}$$

For surfaces with zero skewness, (1.1) reduces to $k_s \approx 4.43\sigma_h$, and therefore $z_0 \approx 0.15\sigma_h$. In the context of geophysical flows, Garratt (1977) report (after Smith & Carson 1977) the approximate relation $z_0 \approx 0.2\sigma_h^2/\lambda_s$, where λ_s is the average distance between dominant orographic modes. For ABL flows over homogeneous terrain, Brutsaert (2005) mentions $z_0 = h_0/10$, where h_0 is a characteristic height of the roughness elements; Tsai & Tsuang (2005) report experimental data which support this value (i.e. $z_0 \approx 5$–$10\,\%$ of mean surface element height) for ABL flows over urban roughness elements where obstacles are close together, and also over rice fields with urban roughness elements more sparsely distributed. They also report values for surface r.m.s. which suggest $z_0 \approx 0.01\sigma_h - 0.2\sigma_h$. There are a number of other proposals for functional relations between geometric and hydrodynamic roughnesses. This suggests that expressing hydrodynamic roughness as the product of a *universal* non-dimensional pre-factor and a surface geometric statistic is by itself unlikely to be successful, and that some type of surface- and flow-dependent determination is necessary.

Now consider the LES context, when a low-pass-filtered range of landscape fluctuations is resolved. A generalization of the classical approach of setting z_0 proportional to the overall height r.m.s. is to set the SGS roughness height $z_{0,\Delta}$ proportional to the local r.m.s. of the unresolved part of the height fluctuations, i.e.

$$z_{0,\Delta} = \alpha\sigma_h^{\Delta}, \quad \text{where} \quad \sigma_h^{\Delta}(x, y) = (\widetilde{h^2} - \tilde{h}^2)^{1/2} \tag{1.2}$$

is the local r.m.s. within a $\Delta \times \Delta$ subarea. The challenge still remains to specify physically meaningful values for α, which will be denoted as the (dimensionless) roughness parameter. For surfaces with broadband height fluctuations, the lack of scale separation implies that the flow at scales slightly larger than the filter scale may interact with the largest unresolved surface features in complicated ways. As already concluded above for the case of fully unresolved roughness elements, it is unlikely

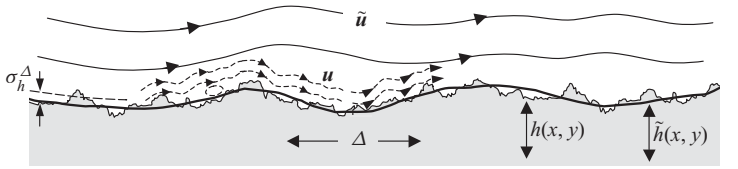

FIGURE 2. Illustrative sketch showing a one-dimensional transect of a multiscale surface over which turbulent flow is simulated using LES. The bold line shows the height of the surface, filtered at scale Δ. Streamlines of the unfiltered ($\boldsymbol{u}$) and filtered ($\tilde{\boldsymbol{u}}$) velocity fields are also shown. The SGS part of the surface defines a local r.m.s. value σ_h^{Δ}.

that a single *universal* value of α would apply to different surfaces, even in the context of LES with parts of the surface resolved.

In this paper, a self-consistency condition is proposed to dynamically determine α based on filtering surface forces at various scales and requiring that the total drag force (momentum flux) be independent of filter scale or resolution. This self-consistency condition is inspired by the Germano identity (Germano 1992) traditionally used to determine model parameters for closing SGS stresses in the bulk of the flow (Germano *et al.* 1991). We call this the dynamic surface roughness (DSR) model. It is developed in § 2. Section 3 presents the LES code and simulation details, while § 4 presents the various rough surfaces to be used in LES tests. Results and self-consistency tests are presented in § 5. Concluding remarks and future perspectives are summarized in § 6.

2. Dynamic surface roughness model

A surface described with multiscale height distribution $h(x, y)$ contains fluctuations over a large range of length scales. In real environmental terrains, such fluctuations range over many orders of magnitudes, from millimetres to kilometres. We assume that when simulating flow over a multiscale surface, $h(x, y)$ will be defined to some very high resolution, Δ_s (e.g. the geospatial resolution available in a GIS database). This scale is assumed to be significantly finer than the LES resolution, Δ, with which one is able to simulate the flow. Our attempt to represent hydrodynamic effects of the full range of surface scales, from the LES horizontal domain size, L, to Δ_s, relies upon spatially filtering the surface at the LES grid-filter width. The filtered height distribution is $\tilde{h} = G_\Delta * h$, where $(*)$ denotes spatial convolution and G_Δ is a horizontal filter with characteristic length scale, Δ, comparable with (or equivalent to) the horizontal grid-spacing to be used in LES. Figure 2 illustrates a sample transect from a rough surface, where we indicate both the unfiltered ($\boldsymbol{u}$, h) and filtered ($\tilde{\boldsymbol{u}}$, $\tilde{h}$) simulation variables (where $\widetilde{(\ldots)}$ denotes filtering at LES resolution, Δ). Fine-grained (direct numerical) simulations would be required to resolve the small-scale pressure and viscous drag effects associated with the smallest-scale velocity features, indicated by dashed streamlines.

The total force acting on the fluid due to the surface is given by

$$F_i = -\int_S \tilde{p}^w \, \tilde{n}_i \, \mathrm{d}S + \rho \int_S \tau_{ij}^{w,\Delta} \, \tilde{n}_j \, \mathrm{d}S, \tag{2.1}$$

where $\tilde{n}_i$ is the unit normal vector to the filtered surface $\tilde{h}(x, y)$ and $\tilde{p}^w$ is the resolved wall pressure. The (kinematic) wall stress $\tau_{ij}^{w,\Delta}$ represents pressure drag forces associated with the unresolved SGS roughness modes all the way down to

the smallest scale Δ_s. It is assumed that the Reynolds number is sufficiently large to ensure that viscous drag at scales Δ_s and larger may be neglected (fully rough surfaces).

In order to model the momentum fluxes associated with the SGS height fluctuations, we invoke the equilibrium log-law assumption which, for neutrally stratified flow, expresses the kinematic wall stress tensor in terms of the resolved velocity nearest to the surface according to

$$\tau_{i3}^{w,\Delta}(x,y) = -\left[\frac{\kappa U^{\Delta}(x,y)}{\log\left(\dfrac{\Delta_z/2-d}{z_{0,\Delta}}\right)}\right]^2 \frac{\widetilde{u}_i(x,y,\Delta_z/2)}{U^{\Delta}(x,y)}, \tag{2.2}$$

where $i=1,2$, and $\widetilde{u}_i(x,y,\Delta_z/2)$ is the local instantaneous velocity at the first grid-point above the surface ($z=\Delta_z/2$, for a staggered grid computational model), d is the displacement height (Kaimal & Finnigan 1994) and will be set equal to the resolvable height field $d(x,y)=\tilde{h}(x,y)$, and κ is the von Kármán constant ($\kappa=0.4$). Also, $z_{0,\Delta}$ is the hydrodynamic roughness length, and

$$U^{\Delta}(x,y) \equiv \left[\widetilde{u}_1(x,y,\Delta_z/2)^2 + \widetilde{u}_2(x,y,\Delta_z/2)^2\right]^{1/2} \tag{2.3}$$

is the local instantaneous resolved horizontal velocity magnitude at scale Δ, at the first vertical grid point. As an aside, we note that when computing the stress that will be substituted into the LES ((3.2), § 3), the velocity field in (2.2) and (2.3) is test-filtered (i.e. $\widetilde{u}_i(\Delta_z/2) \to \widehat{\widetilde{u}}_i(\Delta_z/2)$, $i=1,2$, where $\widehat{(\widetilde{\ldots})}$ denotes test-filtering at a scale 2Δ). As shown in Bou-Zeid, Meneveau & Parlange (2005), this approach is advantageous to remove excessive velocity fluctuations that decrease the accuracy of the log law.

As summarized in § 1, the main challenge is to model the roughness length by specifying an appropriate roughness parameter α in the expression $z_{0,\Delta}=\alpha\sigma_h^{\Delta}$. In order to regularize the expression in the limit of negligible roughness ($\sigma_h^{\Delta}=0$) when substituting in the logarithm, a slightly different expression is used, namely

$$z_{0,\Delta} = \left[z_{0,s}^2 + \left(\alpha\sigma_h^{\Delta}\right)^2\right]^{1/2}, \tag{2.4}$$

where $z_{0,s}$ is a roughness associated with scales even smaller than those to which $h(x,y)$ is originally prescribed at scale Δ_s (it could also be proportional to the viscous roughness length, i.e. $z_{0,s}=c\ \nu/u_*$ for finite-Reynolds-number flows where viscous drag effects would be present). The expression (2.4) is formed such that the variances of the heights at various scales are additive. The roughness parameter α is in principle unknown, allowing the hydrodynamic roughness to differ from the known, local SGS geometric height r.m.s. at scale Δ. One expects α to depend on flow physics and geometric properties of the surface. In this work, only cases in which $z_{0,s} \ll \alpha\sigma_h^{\Delta}$ will be considered, so that the precise value of $z_{0,s}$ is not physically important but numerically convenient.

The main step in determining the roughness parameter α is based on rewriting (2.1) at scale 2Δ, i.e. at a 'test-filter' scale. Based on the requirement that the total drag force must be independent of the resolution chosen to formulate the model, the following identity must hold:

$$-\int_S \tilde{p}^w\ \tilde{n}_i\,\mathrm{d}S + \rho\int_S \tau_{ij}^{w,\Delta}\ \tilde{n}_j\,\mathrm{d}S = -\int_S \widehat{\tilde{p}}^w\ \widehat{\tilde{n}}_i\,\mathrm{d}S + \rho\int_S \tau_{ij}^{w,2\Delta}\ \widehat{\tilde{n}}_j\,\mathrm{d}S. \tag{2.5}$$

Replacing the assumed model for the total drag (2.1) at two scales, considering instead equivalence of total wall stress, and assuming that the resolved height distribution has small enough slopes so that $\tau_{i3}^{w,\Delta}$ is the dominant wall stress component, the self-consistency condition emerges:

$$\frac{1}{\rho}\langle\tilde{p}^{w}\tilde{n}_i\rangle+\left\langle\left[\frac{\kappa U^{\Delta}}{\log\left(\dfrac{\Delta_z/2-\tilde{h}}{z_{0,\Delta}}\right)}\right]^2\frac{\widetilde{u}_i}{U^{\Delta}}\right\rangle=\frac{1}{\rho}\langle\widehat{\widetilde{p}}^{w}\,\widehat{\widetilde{n}}_i\rangle+\left\langle\left[\frac{\kappa U^{2\Delta}}{\log\left(\dfrac{\Delta_z/2-\hat{\tilde{h}}}{z_{0,2\Delta}}\right)}\right]^2\frac{\widehat{\widetilde{u}}_i}{U^{2\Delta}}\right\rangle, \tag{2.6}$$

where $\langle\cdots\rangle$ indicates two-dimensional plane-averaging. All velocities are written at the height of the first grid point above the surface (e.g. $z=\Delta_z/2$ in a staggered grid code) and the roughness heights at the two scales are given, respectively, by

$$z_{0,\Delta}=\left[z_{0,s}^2+\left(\alpha\sigma_h^{\Delta}\right)^2\right]^{1/2}\quad\text{and}\quad z_{0,2\Delta}=\left[z_{0,s}^2+\left(\alpha\sigma_h^{2\Delta}\right)^2\right]^{1/2}. \tag{2.7}$$

The implicit assumption has been made that the parameter α is scale-invariant (Meneveau & Katz 2000). Also, note that condition (2.6) is enforced in the dominant flow direction (e.g. $i=1$), but other options exist, such as least-square-error minimization over the two vector components. Also, to capture possible spatial variations, one could perform the averaging over smaller subregions of the surface. For the present initial applications and tests, a planar averaging will be performed, appropriate for statistically homogeneous surfaces and flows considered here.

If the resolved pressure forces acting on the surface are known during the simulation, then (2.6) provides an equation that can be solved for the unknown model parameter α since all other variables in (2.6) are known. If the resolved pressure forces acting on the surface are simulated using an immersed boundary method or a surface-gradient approach (see § 3) in which the forces are prescribed using a body force, f_i^{Δ}, near the surface, then in (2.6) a term proportional to $\langle f_i^{\Delta}\rangle$ replaces $\langle\tilde{p}^{w}\tilde{n}_i\rangle/\rho$ at scale Δ, and $\langle f_i^{2\Delta}\rangle$ replaces $\langle\widehat{\widetilde{p}}^{w}\,\widehat{\widetilde{n}}_i\rangle/\rho$ at scale 2Δ.

When filtering at scale Δ, forces are composed of resolved pressure forces acting on the height fluctuations and contributions from the SGS height variations proportional to the local r.m.s. If the same surface is now filtered at the larger test-filter scale 2Δ, the resolved pressure forces are smaller than at scale Δ, due to the smoothed height fluctuations. However, the unresolved local height r.m.s. is larger since more fluctuations are now subgrid, and thus one expects the SGS drag to be larger. The DSR model relies on the condition that there should exist a single roughness parameter α for which the total force (the sum of resolved and SGS drag) is the same at filter and test-filter scales. The next section describes the LES code used in tests of the DSR model.

3. Large-eddy simulation details

The LES code (Albertson & Parlange 1999) solves the incompressible high-Reynolds-number momentum equation in rotational form and the boundary layer is forced with a constant pressure gradient in the streamwise direction:

$$\frac{\partial\tilde{u}_i}{\partial x_i}=0, \tag{3.1}$$

$$\frac{\partial\tilde{u}_i}{\partial t}+\tilde{u}_j\left(\frac{\partial\tilde{u}_i}{\partial x_j}-\frac{\partial\tilde{u}_j}{\partial x_i}\right)=-\frac{1}{\rho}\frac{\partial\tilde{p}}{\partial x_i}-\frac{\partial\tau_{ij}}{\partial x_j}-\frac{1}{\rho}\Pi\delta_{i1}+f_i^{\Delta}. \tag{3.2}$$

In (3.2), $\tilde{p}$ is the modified pressure, f_i^{Δ} is a body force (for example, to represent horizontally resolved height fluctuations using an immersed boundary or surface-gradient model, see below), Π is the imposed constant streamwise pressure-gradient forcing, and therefore in steady-state conditions for fully developed flow,

$$u_*^2 = -\frac{1}{\rho}\Pi H, \tag{3.3}$$

where u_* is the friction velocity and H is the height of the computational domain. Here τ_{ij} is the SGS stress tensor ($\tau_{ij} = \widetilde{u_i u_j} - \widetilde{u}_i \widetilde{u}_j$). In this paper, we consider neutrally stratified flow without the presence of a scalar. Incompressibility is enforced by the pressure Poisson equation, solution of which yields a pressure correction on the velocity field at every time step. Variants of this code have been used extensively in past research efforts, for example Porté-Agel, Meneveau & Parlange (2000), Bou-Zeid *et al.* (2005), Chamecki, Meneveau & Parlange (2009) and Anderson & Meneveau (2010).

The code uses a staggered grid formulation, with the first vertical computational level for $\widetilde{u}_i$ ($i = 1, 2$) placed at height $\Delta_z/2$ from the ground. The code employs pseudo-spectral discretization and evaluation of derivatives in the horizontal directions, while in the vertical direction derivatives are evaluated with centred second-order finite-differencing. The advection term is de-aliased with the 3/2 rule (Orszag 1970). At the domain top, we impose the stress-free boundary condition by imposing $\partial \tilde{u}_i/\partial x_3|_{z/H=1} = 0$ ($i = 1, 2$) and non-penetration condition for the vertical velocity ($\tilde{u}_3|_{z/H=1} = 0$). The horizontal boundary conditions on the vertical faces of the domain are periodic, owing to the use of spectral methods in the horizontal directions. The horizontal domain dimensions are $L_x = L_y = L = 2\pi H$. The number of computation points in each direction are denoted as $N_x = N_y = N_z = N$ (z corresponds to the vertical). The domain is discretized such that $\Delta_x = L_x/N_x$ and $\Delta_y = L_y/N_y$. As the streamwise and transverse grid size is equal, from this point we simplify by specifying $\Delta = \Delta_x = \Delta_y$. For each of the surfaces to be considered (see § 4), we run LES with $N = 32$, 64 and 128. The base hydrodynamic roughness is $z_{0,s}/H = 1 \times 10^{-9}$ (i.e. small enough to be simultaneously negligible while preventing numerical instability for the case of $\sigma_h^{\Delta} = 0$ or $\alpha = 0$, in (2.2)).

The deviatoric part of the SGS stress tensor is expressed using the eddy-viscosity concept as

$$\tau_{ij} - \tfrac{1}{3}\delta_{ij}\tau_{kk} = -2\nu_t \tilde{S}_{ij}, \tag{3.4}$$

where ν_t is the turbulent eddy-viscosity and $\tilde{S}_{ij}$ is the resolved strain-rate tensor. The well-known Smagorinsky model, $\nu_t = [C_S\Delta]^2|\widetilde{S}|$, where C_S is the Smagorinsky coefficient (Smagorinsky 1963), has seen several improvements. Early studies used location-, discretization-, and flow-dependent prescriptions for C_S (Lilly 1966; Deardorff 1970; Mason & Callen 1986; Piomelli, Moin & Ferziger 1988) for simulations in which the turbulence was not fully homogeneous. Germano *et al.* (1991) developed a dynamic tuning-free approach to computing the Smagorinsky coefficient, which was based on filtering the flow variables at two resolutions: Δ and 2Δ, and assuming scale similarity between the information at these resolutions. This approach has been further generalized and applied to other SGS parameterizations (Kosović 1997; Chow *et al.* 2000) and to account for scale dependencies (Porté-Agel *et al.* 2000; Bou-Zeid *et al.* 2005). The SGS model used in this work is the Lagrangian scale-dependent dynamic model, as introduced in Bou-Zeid *et al.* (2005).

Simulations are run with non-dimensional time step, $\Delta t^* = \Delta t u_*/H = 1.8 \times 10^{-4}$, 0.9×10^{-4} and 2.25×10^{-5} for simulations spatially resolved with $N = 32$, 64 and 128, respectively. System variables are non-dimensionalized with domain height, H, and friction velocity, u_*. All LES are run until the flow field stabilizes with respect to various simulation statistics including temporal evolution of kinetic energy.

3.1. *Horizontally resolved drag force using surface-gradient method*

For the application encountered here, where a Cartesian-structured grid is used and the smoothed surface, $\tilde{h}$, falls below the height of the first vertical grid point, $\Delta_z/2$, the SGD model is used to represent an immersed drag force f_i^{Δ} (see (3.2)) corresponding to form drag, as recently shown in Anderson & Meneveau (2010). For simplicity, here we consider cases with equivalent mesh size in the streamwise and transverse directions ($\Delta = \Delta_x = \Delta_y$). The flow in the cell volume nearest to the surface is obstructed by an area normal to the horizontal flow that is equal to the component of $\nabla\tilde{h}\ \Delta$ in the direction of the flow. The corresponding incoming linear momentum flux due to the resolved flow is thus $\rho\tilde{\boldsymbol{u}}(\tilde{\boldsymbol{u}}\cdot\nabla\tilde{h})\ \Delta^2$, and the method relies on adding the volume force near the boundary that will cancel this momentum flux. Dividing by density and local mesh volume, $\Delta V = \Delta^2\Delta_z$, the volume force to be applied to the grid points nearest to the surface ($\Delta_z/2$ in our staggered mesh code) becomes

$$f_i^{\Delta}(x, y, \Delta_z/2) = -\widetilde{u}_i R\left(\widetilde{u}_k \frac{\partial\tilde{h}}{\partial x_k}\right)\frac{1}{\Delta_z}, \tag{3.5}$$

where $\partial\tilde{h}/\partial x_k$ are the horizontal components of the surface gradient ($k = 1, 2$), and the velocities are evaluated at height $z = \Delta_z/2$; $R(x)$ is the ramp function, defined as $R(x) = x$ if $x \geqslant 0$ or 0 if $x < 0$. We consider incoming flow in both the streamwise and transverse directions and specify that the obstacle only causes hydrodynamic drag when the flow component is normal into the obstacle; otherwise, we assume that there is no resolved drag force since on downstream facing surfaces, often involving flow separation, the force is much smaller. In the applications to be considered, we neglect forcing in the vertical direction, i.e. we set $f_3^{\Delta} = 0$. The SGD model has been tested in Anderson & Meneveau (2010) by comparing with a number of data sets in the literature for surfaces with a variety of shapes (Nakayama & Sakio 2002; Bhaganagar *et al.* 2004; Kanda, Moriwaki & Kasamatsu 2004; Coceal *et al.* 2007; Xie, Coceal & Castro 2008), and good agreement was reported.

In the context of this surface-gradient approach, the DSR model (2.6) can be rewritten by replacing the surface integral of pressure force by a volume integral of the body force (i.e. $\int_0^{\Delta_z} f_i^{\Delta}(z)\,\mathrm{d}z \approx f_i^{\Delta}(\Delta_z/2)\Delta_z$); thus,

$$\left\langle \widetilde{u}_i R\left(\widetilde{u}_k \frac{\partial\tilde{h}}{\partial x_k}\right)\right\rangle + \left\langle \left[\frac{\kappa U^{\Delta}(x, y)}{\log\left(\dfrac{\Delta_z/2 - \tilde{h}}{z_{0,\Delta}}\right)}\right]^2 \frac{\hat{\widetilde{u}}_i}{U^{\Delta}}\right\rangle$$
$$= \left\langle \widehat{\widetilde{u}}_i R\left(\widehat{\widetilde{u}}_k \frac{\partial\hat{\tilde{h}}}{\partial x_k}\right)\right\rangle + \left\langle \left[\frac{\kappa U^{2\Delta}(x, y)}{\log\left(\dfrac{\Delta_z/2 - \hat{\tilde{h}}}{z_{0,2\Delta}}\right)}\right]^2 \frac{\hat{\hat{\widetilde{u}}}_i}{U^{2\Delta}}\right\rangle. \tag{3.6}$$

Note that in rewriting the SGS drag term at both scales, we follow the approach of Bou-Zeid *et al.* (2005) by using the test-filtered velocity in the log law (thus, $\widetilde{\widetilde{\ldots}}$ denotes filtering at twice the test-filter width, 4Δ), and $U^{2\Delta}$ is defined according to

$$U^{2\Delta}(x, y) \equiv \left[\widetilde{\widetilde{u}}_1\left(x, y, \frac{\Delta_z}{2}\right)^2 + \widetilde{\widetilde{u}}_2\left(x, y, \frac{\Delta_z}{2}\right)^2\right]^{1/2}. \tag{3.7}$$

Unlike in applications of the Germano identity to the standard Smagorinsky model (Germano *et al.* 1991), where algebraic manipulation leads to the well-known explicit expression for C_S (thereby simplifying dynamic computations), here the unknown α enters inside a transcendental function (logarithm). This makes solution more challenging. The bisection solution-finding algorithm is used at each time step of the LES to solve α (the bisection method solution interval limits, $[a, b]$, are initially set to $a = 0$ and $b = 1$, and solutions are always found in this interval in our simulations). With α computed, the effective roughness can subsequently be computed with (2.4) and substituted into (2.2) ($i = 1, 2$), for subsequent use at the next time step.

Simulations are initialized from a logarithmic mean velocity profile to which random numbers (white noise) are added with a prescribed kinetic energy profile. These attenuate quickly and physically realistic turbulence develops. To preserve numerical stability of the DSR model, an initialization period of 1000 time steps is used in which the SGS roughness parameter is 'statically' specified as $\alpha = 0.3$ (we have found this measure to be somewhat conservative and in most cases it could be relaxed; in any case, we add that 1000 time steps represents approximately 0.5 % of the total number of LES time steps necessary to converge the flow). Once the dynamic model is activated and the dynamic α values are used at the next time step, results show that the parameter converges to its final value rapidly. This is found even for cases where the dynamic (solution) α is several orders of magnitude different from the initial static value. Furthermore, it has been independently verified that using different values of static α for initialization: (i) makes negligible difference to the subsequent dynamic evolution of α and (ii) does not affect the rate of convergence of α.

4. Rough surface cases

In order to test the DSR model in LES of flow over surfaces with scale-invariant height distribution, we consider isotropic synthetic surfaces built using the random Fourier modes (RFM) method with power-law height spectra. The surfaces are constructed as follows:

$$h(\boldsymbol{x}) = \sum_{\boldsymbol{k}} c k^{1/2(\beta_s - 1)} \mathrm{e}^{\mathrm{i}(\boldsymbol{k}\cdot\boldsymbol{x} + \varphi)}. \tag{4.1}$$

In the above, c is an amplitude (adjusted as described below), β_s is the spectral slope, and φ is a random phase shift between 0 and 2π and chosen from a uniform distribution for each horizontal wavenumber $\boldsymbol{k}$. In this work, RFM surfaces are built with spectral slopes $\beta_s = -1.2$ (most rough), -1.6, -2.0, -2.4 and -3 (most smooth). The choice of these β_s values serves two purposes: (i) to build landscapes that cover a range of statistics that are similar to those often encountered in geophysical flows, such as evolved fluvial landscapes where $\beta_s = -2.0$ is common (Passalacqua *et al.* 2006) or the developed wind-driven ocean surface where $\beta_s = -3.0$ has been reported (Phillips 1958); and (ii) to provide a framework for parametric tests on the dependence between β_s and the SGS roughness parameter, α. Applying Orey's formula (Orey

1970; Mandelbrot 1982) that relates fractal dimension D of a self-affine surface to the spectral exponent, $D=(7+\beta_s)/2$, the range $-3.0\leqslant\beta_s\leqslant-1.2$ corresponds to a range of surface fractal dimensions of $2\leqslant D\leqslant 2.9$. Note that we do not consider rougher surfaces (β_s larger than -1.2) to avoid approaching $\beta_s=-1$, which is ill-defined. This issue arises because $[\sigma_h^{\Delta}]^2=\int_{\pi/\Delta}^{\infty}E_h(k)\mathrm{d}k$ and thus the SGS height variance would diverge with small-scale cutoff for $\beta_s\geqslant-1$. Also, the corresponding fractal dimension would indicate a 'space-filling' surface ($D=3$), which reaches the limit of validity of Orey's formula.

It is useful to recall that the spectral density of the gradients of the height (surface slope) is $k^2E_s(k)$ and therefore it scales with an exponent $2+\beta_s$. Since the variance of the gradient is the integral of the spectrum, for any $\beta_s\geqslant-3$ the variance of the gradient will be dominated by the small scales (ultraviolet divergence). Thus, even for the smoothest surfaces considered here, the most dominant contributions to gradients occur at the smallest scales. This is consistent with the assumption that the drag forces consist of pressure (form) drag at all scales, down to the smallest scales.

In the numerical experiments, synthetic landscapes are built using high resolution, using $N_x\times N_y=1024\times1024$. These fine-grained surfaces are processed in order to obtain (unfiltered) surfaces that all have the same mean height and variance. The processing is accomplished as follows. Starting with the unfiltered height distribution $h(x,y)$ obtained from (4.1), the mean height is subtracted and the result is divided by its overall r.m.s. and multiplied by $\frac{1}{4}\Delta_z^{min}$, where Δ_z^{min} is the vertical mesh spacing of the highest resolution case we consider, with $N=128$. The height distribution now has zero mean and r.m.s of $\frac{1}{4}\Delta_z^{min}$. In order to ensure that (typically) all peaks and valleys fall within $\pm\frac{1}{4}\Delta_z^{min}$, the heights are divided again by a factor of $\xi=2.75$. We finally add $\frac{1}{4}\Delta_z^{min}$. Thus, all (unfiltered) surfaces have the same mean height and r.m.s., irrespective of β_s. For inclusion as boundary condition in LES, we apply a spatial box filter of size Δ to create the $\tilde{h}$ surfaces which can be horizontally resolved in the LES computational mesh (with the SGD model). It is then tested that the resulting surfaces all satisfy $0<\tilde{h}<\Delta_z/2$ at every point in the domain, for the $N=128$ case. The two coarser resolutions, $N=32$ and 64, trivially comply with this constraint since $\Delta_z/2$ for these N is four times and double the value for $N=128$, respectively. In the context of LES of the ABL, if the domain height corresponds to 1.5 km (such as in typical LES of micro-meteorological processes), the grid scales $\Delta=2\pi H/N$ used here would correspond to 300, 150 and 75 m, approximately.

Figure 3 shows images of the synthetic surfaces generated. For visualization purposes the vertical and horizontal scaling is not the same (vertical direction has been very much stretched to see the roughness elements). We show the two extreme cases considered, with figure 3(a) illustrating a very rough surface with $\beta_s=-1.2$ and figure 3(b) showing the smoothest surface considered, with $\beta_s=-3.0$. An intermediate roughness case for $\beta_s=-2.0$ has already been shown in figure 1. The range of spectral slopes $-1.2\leqslant\beta_s\leqslant-3$ considered in this paper offers a meaningfully wide range that encompasses realistic terrains around the often observed $\beta_s=-2$ case (for evolved fluvial landscapes). Radial height spectra measured directly from the synthetic surfaces are shown in figure 4. By design, the RFM surfaces must exhibit height power-law spectra, $E_h(k)\sim k^{\beta_s}$.

Figure 5 presents important statistical and extreme-value properties of the RFM surfaces as a function of β_s, for the three LES resolutions considered. By construction, the average filtered height $\langle\tilde{h}\rangle/H$ is constant across the range of spectral slopes considered. The maximum and minimum values of $\tilde{h}/H$ do not change significantly across β_s, though we note an increase in maximum $\tilde{h}/H$ between the $N=32$ and

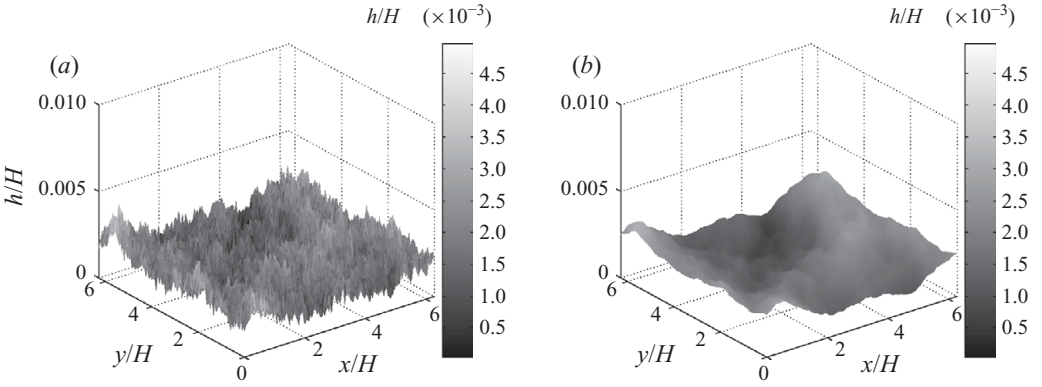

FIGURE 3. Visualization of the fine-grained (1024×1024) multiscale landscape built with the RFM method: (*a*) $\beta_s = -1.2$ and (*b*) $\beta_s = -3.0$.

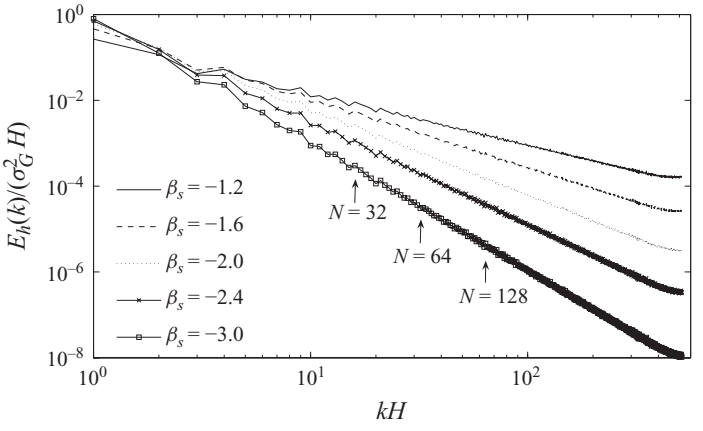

FIGURE 4. Radial spectra of RFM surfaces for spectral exponent values indicated in the figure. Energy normalized by square of the global r.m.s. of the fine-grained surface, σ_G^2. Vertical arrows indicate LES grid-filter wavenumbers π/Δ for the three spatial resolutions considered in this work.

$N = 128$ surfaces in figures 5(*a*) and 5(*c*), respectively. This is expected, as decreasing filter width Δ reduces smoothing and results in more surface topography modes being resolved. To this extent, we note the significant change in the plane-averaged norm of the resolved surface streamwise first-order derivative $\langle|\partial_1\tilde{h}|\rangle$ between resolutions (note that the transverse gradient $\langle|\partial_2\tilde{h}|\rangle$ is of similar magnitude, consistent with the surface isotropy imposed by the construction method, (4.1)). Similarly, the plane-averaged normalized r.m.s. $\langle\sigma_h^{\Delta}\rangle/H$ varies as expected across the different resolutions, being largest for $N = 32$ (figure 5*a*) and decreasing with finer resolution.

5. Large-eddy simulation results

Results from LES with the DSR model are presented for flow over the five different RFM surfaces. Mean velocity profiles are shown in § 5.2 and some important representative second-order velocity statistics are reported in § 5.3

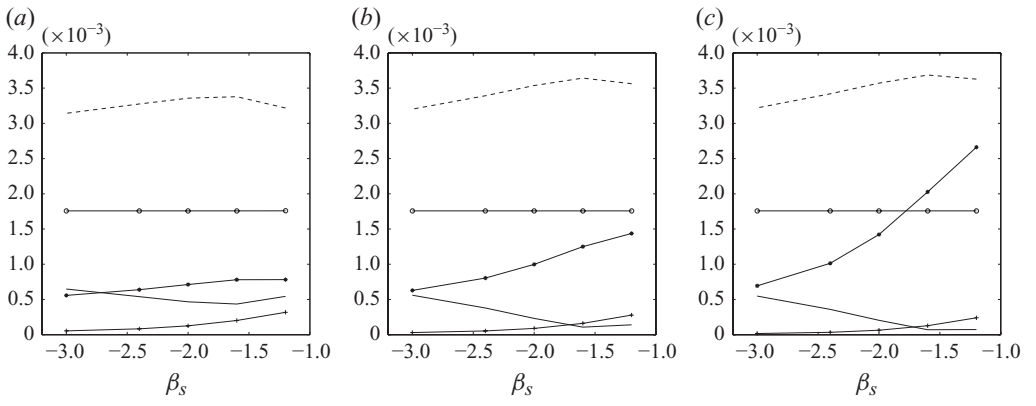

FIGURE 5. Statistical and extreme values of the synthetic RFM surfaces as a function of spectral slope β_s and resolution for different LES resolutions: (*a*) $N = 32$, (*b*) $N = 64$ and (*c*) $N = 128$. ○, mean height ($\langle\tilde{h}\rangle/H$); dashed line, maximum value of the filtered height ($\max[\tilde{h}]/H$); solid line, minimum value of the filtered height ($\min[\tilde{h}]/H$); +, mean of the SGS r.m.s. ($\langle\sigma_h^{\Delta}\rangle/H$); ∗, mean magnitude of the resolved slope ($\langle|\partial_1\tilde{h}|\rangle$).

5.1. *SGS roughness parameter*

As outlined in § 3.1, the DSR model evaluates the SGS roughness parameter α during LES with the bisection method. For the $N = 32$ cases, figure 6 illustrates how the two components of the drag force (drag based on log law, (2.2), and resolved force due to SGD model contribution, (3.5)) vary with respect to α, and how the solution occurs when the total wall stress, $-\langle\tau_{13}^{T}\rangle$, is equivalent at the grid- and test-filter scale. The total (superscript T) kinematic wall stress at scale Δ is, in this application, defined according to

$$-\left\langle\tau_{13}^{\Delta,T}(\alpha)\right\rangle = -\left\langle f_1^{\Delta}\right\rangle\Delta_z - \left\langle\tau_{13}^{w,\Delta}(\alpha)\right\rangle$$
$$= \left\langle\widetilde{u}_1 R\left(\widetilde{u}_k\frac{\partial\tilde{h}}{\partial x_k}\right)\right\rangle + \left\langle\left[\frac{\kappa U^{\Delta}(x,y)}{\log\left(\dfrac{\Delta_z/2-\tilde{h}}{z_{0,\Delta}}\right)}\right]^2\frac{\hat{\widetilde{u}}_1}{U^{\Delta}}\right\rangle. \quad (5.1)$$

A similar equation is written at scale 2Δ (the right-hand side of (3.6)) and thus the dynamic approach can also be written as $\langle\tau_{13}^{\Delta,T}(\alpha)\rangle = \langle\tau_{13}^{2\Delta,T}(\alpha)\rangle$. In practice and in this paper, planar averaging is used without time averaging. More spatially localized versions of the model can be envisioned, but in this first application we opt for the simplest approach of horizontal averaging; we also note that this is somewhat similar to Germano *et al.* (1991), who used planar averaging to maintain numerical stability when dynamically evaluating C_S in LES of turbulent channel flow. This approach is consistent with the surfaces and flows considered with planar statistical homogeneity.

The SGS part of the total stress depends on the α value. Shown in figure 6 is the instantaneous total plane-averaged wall stress evaluated from simulation at a particular time, for three of the surface spectral slopes considered. The stress shown here is evaluated as a function of the parameter α. With increasing α, the roughness and the wall stress $\langle\tau_{13}^{w,\Delta}(\alpha)\rangle$ increases. The total stress at scale 2Δ may also be evaluated as a function of α. Here $\langle\tau_{13}^{w,2\Delta}(\alpha)\rangle$ is larger than at scale Δ and also increases with α, and more quickly. However, the resolved part of the stress is smaller.

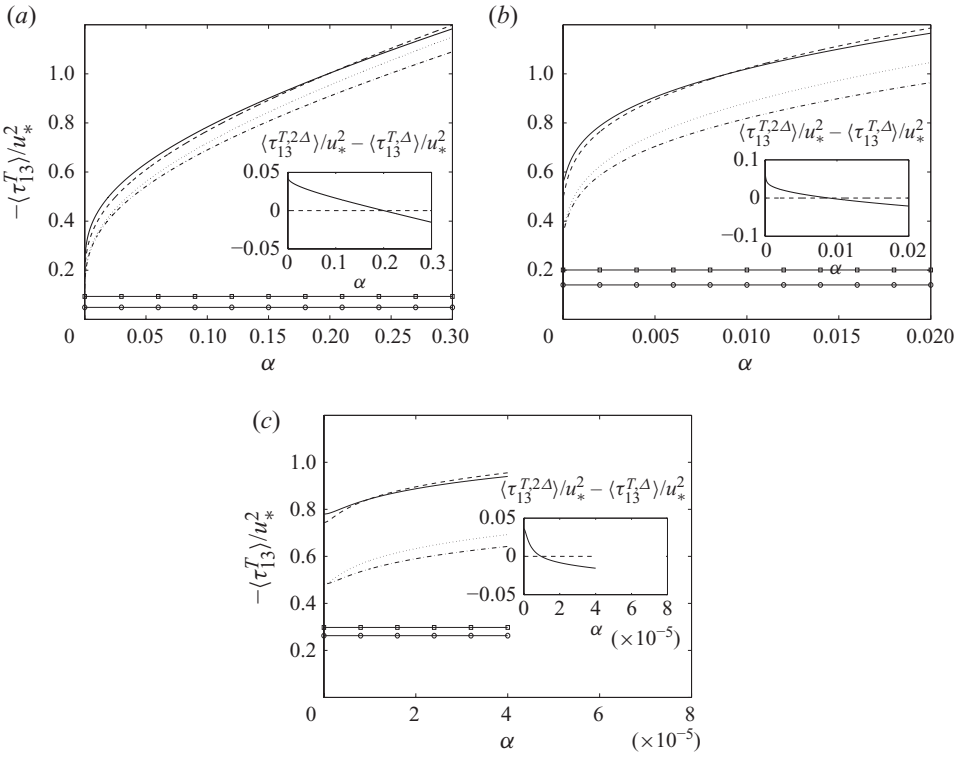

FIGURE 6. Value of individual and total wall stress components (SGS and resolved) as a function of the roughness parameter α. Results are shown for both grid-filter scale Δ and test-filter scale 2Δ. Lines and symbols: solid line, $\langle\tau_{13}^{T,\Delta}\rangle$; dashed line, $\langle\tau_{13}^{T,2\Delta}\rangle$; dot-dashed line, $\langle\tau_{13}^{w,\Delta}\rangle$; dotted line, $\langle\tau_{13}^{w,2\Delta}\rangle$; □, $\langle f_1^{\Delta}\rangle\Delta_z$; ○, $\langle f_1^{2\Delta}\rangle\Delta_z$. The insets show the total wall stress difference whose zero crossing indicates the value of α that yields self-consistency across scales where the mean total stresses at two scales are equal. Different plots correspond to different spectral slopes, namely (*a*) $\beta_s = -1.2$, (*b*) $\beta_s = -2.0$ and (*c*) $\beta_s = -3.0$. These profiles are from the $N = 64$ cases.

As a result, for a particular value of α both curves cross, and this is the solution for α sought using the bisection algorithm, at each time step of the simulation. The α value found as a solution is then used to evaluate the wall stress during the next time step.

Since the simulations reach statistically steady conditions, the correct solution for each case shown in figure 6 is when $-\langle\tau_{13}^T\rangle/u_*^2 \approx 1$, indicating that the total stress balances the imposed pressure gradient. One can also appreciate that the contribution from the SGD model increases for decreasing spectral slope (smoother surfaces), consistent with the expectation that drag effects of smoother surfaces are more strongly affected by the gradient $\nabla\tilde{h}$ (3.5) than by the SGS portion. In some cases (e.g. figure 6*a*), the solution of $\langle\tau_{13}^{T,\Delta}\rangle = \langle\tau_{13}^{T,2\Delta}\rangle$ is difficult to observe and the insets show more clearly where the solution occurs. Corresponding plots for the other β_s cases considered and those at other resolutions ($N = 32$ and $N = 128$) are very similar (and omitted here for brevity).

Figure 7 shows time series of α during the simulation, for the LES using $N = 64$ resolution. The corresponding surface spectral slopes are indicated in the legend while N_t denotes LES time step. The figure shows that α converges very quickly,

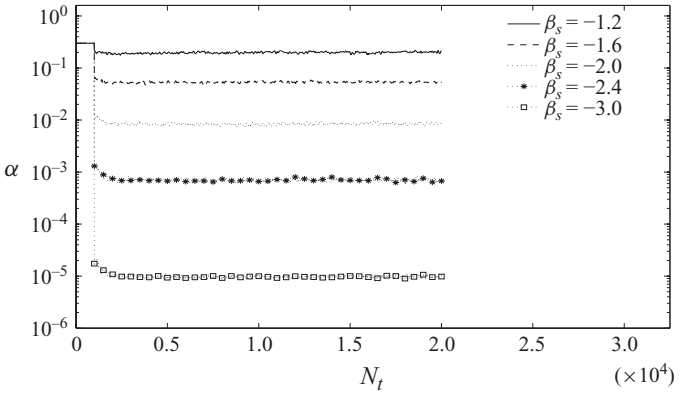

FIGURE 7. Typical time series of the SGS roughness parameter as a function of time step for $N = 64$ LES and the five spectral slopes, following activation of the dynamic model after 1000 time steps. Only the first 20 000 time steps are shown. The time step is $\delta t = 1.8 \times 10^{-4} H/u_*$.

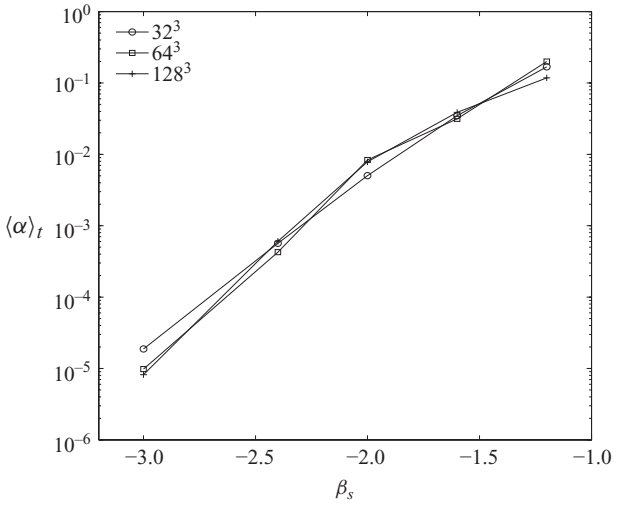

FIGURE 8. Time-averaged SGS roughness parameter α as a function of the surface spectral exponent ($\langle\cdots\rangle_t$ denotes temporal average).

much faster than the velocity field, to the final value around which it fluctuates, as soon as the dynamic model is activated ($N_t > 1000$). No undesirable instabilities are observed and the behaviour of the model is extremely robust. As a result, no clipping of the parameter α is required. In large part this robust behaviour is related to the planar-averaging process. In terms of the values of the parameter, it is observed that for each decrement of β_s by -0.4, α decreases by approximately an order of magnitude.

For all cases, the temporally averaged α are shown in figure 8 as a function of spectral exponent and for the three resolutions considered. Temporal averages are taken for the final 30 % of the simulation (typically over 70 000 time steps). A strong dependence of α on spectral slope is evident, while dependence on resolution is quite small. This serves as an *a posteriori* verification of the scale-invariance assumption, in which it was assumed that α should not depend upon filter scale owing to the lack of

characteristic scale in a multiscale surface with power-law spectrum interacting with a very high Reynolds number turbulent flow.

5.2. *Mean velocity profiles*

In order to validate the dynamic approach, comparisons to high-resolution data would be desirable. Due to the challenges of finding experimental or field data at Reynolds numbers high enough and of sufficient accuracy for flow over rough surfaces with known power-law surface height spectrum, a computational approach is chosen for testing the accuracy of the DSR model. To use simulation data, one would like to perform simulations with high resolution and compare with LES at coarse resolutions. Using DNS with viscous effects included to simulate a reference case with sufficient range of scales against which LES could be meaningfully compared would be prohibitive: a numerical simulation would need to resolve length scales ranging from the flow viscous scale and corresponding surface height fluctuations (i.e. sub Δ_s), to surface length scales defining the largest height fluctuations that would be at least several orders of magnitude larger than Δ_s. Conversely, one may consider high-resolution LES in which some of the roughness is modelled using an effective roughness height, i.e. specifying a particular value of z_0 or α. For instance, one may perform N_1^3 LES and compare with N_2^3 LES (with $N_2 \ll N_1$) and test whether the mean velocity profiles coincide, i.e. if the SGS surface parameterization in the coarse-scale LES effectively captures the additional drag that arises from the height fluctuations between the N_1 and N_2 resolutions. Instead of specifying some particular value of α for the fine-scale LES, one may use the dynamically computed α value. Such comparison then reverts to comparing the dynamic LES at various resolutions and testing whether the mean velocity (shift, ΔU) is independent of the LES resolution. Then, one may also test whether such independence is observed when using non-dynamic, arbitrarily specified values of α.

In fact, to fully motivate the DSR model in the context of achieving resolution-independent predictions, it is firstly of interest to perform 'no-model' simulations by setting $\alpha = 0$ in (2.4). Drag is then exclusively imposed by resolvable roughness modes (through the SGD model, f_i^{Δ}, (3.5)), and increasing resolution (N) increases the range of roughness modes resolved by the SGD drag model. Results are shown in figure 9. As expected, vertical profiles of streamwise velocity are subjected to increased drag with increasing resolution and no resolution-independent mean velocity profiles are obtained. This disagreement (or resolution-dependence) between velocity profiles for different N clearly highlights the need for a model for the unresolved roughness effects.

Figure 10 shows the plane- and time-averaged streamwise ($i = 1$) velocity profiles for LES with drag effects modelled with the DSR model. Runs with different resolutions are indicated using different symbols. There are five groups of curves, each with three lines for the three resolutions considered. The different β_s are indicated at the far right of the plot. As a reference, also shown is the log law to be expected with only the base-line roughness $z_{0,s}$ (dashed line). As can be expected, the velocity profile shifts downwards for increasing β_s, indicating more drag imposed with rougher surfaces. Comparisons of the mean velocity profiles focus on the more universal log-layer region, at $z/H \lesssim 0.15$. Further away from the surface the details of the mean profile depend on the boundary condition used in the upper parts of the domain. For instance, we observe that the present simulations based on 'half-channel boundary conditions' yield less of a wake behaviour as compared to that in developing turbulent boundary layers.

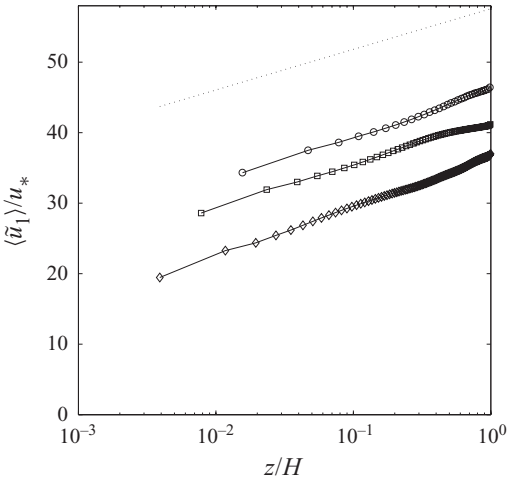

FIGURE 9. Non-dimensional mean streamwise velocity profiles in semi-logarithmic scale for the RFM surface for $\beta_s = -1.2$ with no model for unresolved roughness modes. Increasing resolution increases the range of resolved roughness modes (modelled with f_i^{Δ}, (3.5)), as expected. Lines and symbols: dotted line, logarithmic profile $(1/\kappa)\log(z/z_0)$ for $z_0 = z_{0,s}$; ○, LES with $N = 32$; □, LES with $N = 64$; ◇, LES with $N = 128$.

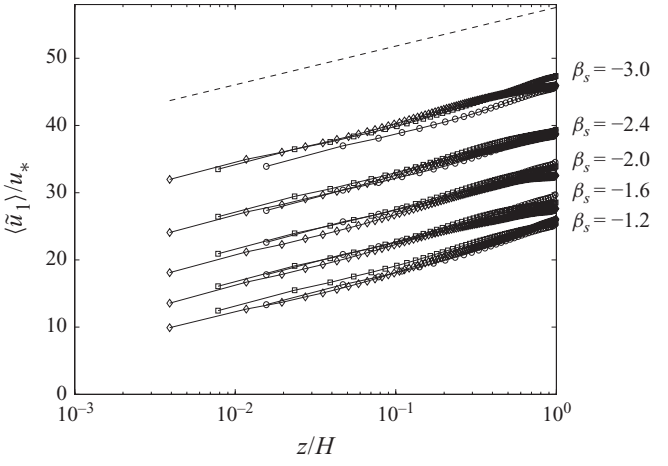

FIGURE 10. Non-dimensional mean streamwise velocity profiles in semi-logarithmic scale for RFM surfaces with spectral slopes indicated on right of the figure, using the dynamic roughness model; dotted line, logarithmic velocity for $z_{0,\Delta} = z_{0,s}$; ○, $N = 32$; □, $N = 64$; ◇, $N = 128$.

In comparing the results for different resolutions, quite good agreement in the velocity profiles can be observed for each of the different roughness cases. The model adjusts to changing resolutions by exchanging resolved drag with unresolved drag. The dynamically obtained α is the (unique) value that causes such consistent behaviour, precisely because it has been obtained from the self-consistency condition applied to the total mean wall stress. Hence, the velocity shift in the log layer is approximately independent of the resolution. Minor differences (typically less than 8 %–10 %) are still visible between resolutions, but these differences are much smaller than those obtained when using $\alpha = 0$ (figure 9). In figure 11, we show what happens if for the $\beta_s = -1.2$ and $\beta_s = -3.0$ surfaces we use a static (non-dynamic)

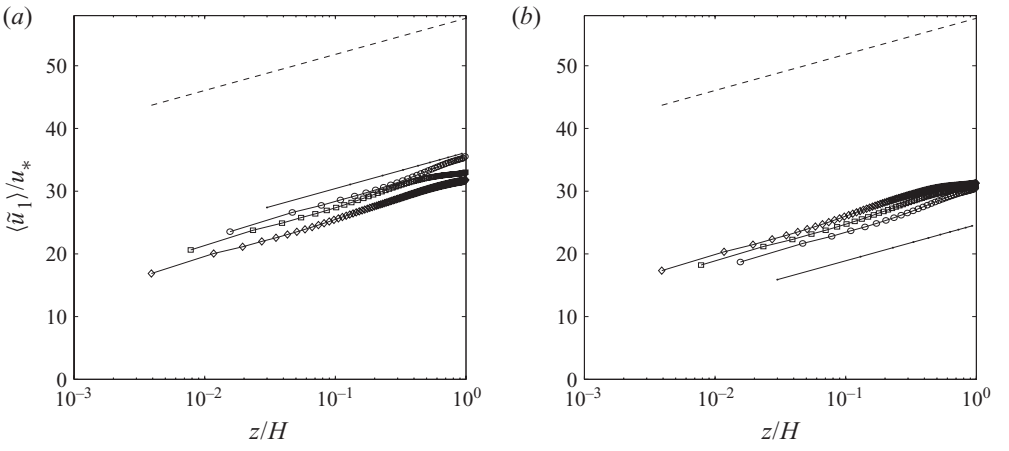

FIGURE 11. Non-dimensional mean streamwise velocity profiles in semi-logarithmic scale for RFM surface for (*a*) $\beta_s = -1.2$ and (*b*) $\beta_s = -3.0$, but using a non-dynamic (static) value of $\alpha = 0.001$ in (*a*) and $\alpha = 0.1$ in (*b*). Results show significant dependence on resolution when a static α specified is different from that obtained by the dynamic condition, highlighting the importance of using the correct value of α for a given surface. Dotted line, logarithmic profile $(1/\kappa)\log(z/z_0)$ for $z_0 = z_{0,s}$; solid line, logarithmic profile for $z_0 = z_{0,G} = (z_{0,s}^2 + (\alpha\sigma_G)^2)^{1/2}$, where $\sigma_G = (\langle h^2 \rangle - \langle h \rangle^2)^{1/2}$ is the overall r.m.s. of the rough surface and again, $\alpha = 0.001$ in (*a*), and $\alpha = 0.1$ in (*b*); ○, LES using $N = 32$; □, LES with $N = 64$; ◇, LES with $N = 128$.

α different from that obtained by application of the dynamic approach. For $\beta_s = -1.2$ and $\beta_s = -3.0$, we impose $\alpha = 0.001$ and $\alpha = 0.1$, respectively, for each of the resolutions. It can be observed that velocity profiles no longer agree at different resolutions. Since the α value prescribed for the $\beta_s = -1.2$ case is too small compared to the dynamic value, as one coarsens the grid, the SGS part of the drag is less than it should be and the velocity profile continues to shift upwards. Stated differently, refining the grid does not lead to a converged solution and the profiles shift downwards. Conversely, for the $\beta_s = -3$ case, in which the specified α is too large compared to the dynamic value, refining the grid yields continuing upward shifts of the mean velocity, and again there is no indication of convergence as a function of scale. In both cases, if the entire roughness was modelled using the equilibrium log law with a roughness scale $z_{0,G} = (z_{0,s}^2 + (\alpha\sigma_G)^2)^{1/2}$, one could obtain the log law $\langle \tilde{u}_1(z) \rangle / u_* = (1/\kappa)\log(z/z_{0,G})$ indicated by a solid line. Here $\sigma_G = (\langle h^2 \rangle - \langle h \rangle^2)^{1/2}$ is the overall r.m.s. of the rough surface. As can be observed, the various LES differ more and more from this value at increasing resolution. This is a clear indication that the prescribed values of α are unrealistic.

Alternatively, a comparison with the global roughness height that models the entire roughness can be made using the dynamically computed α to construct a log-law profile with $z_{0,G} = (z_{0,s}^2 + (\langle \alpha \rangle_t \sigma_G)^2)^{1/2}$. In figure 12 this global log law (solid lines) is compared to the $N = 128$ LES. The agreement is very good (the largest discrepancy occurs for the $\beta_s = -3.0$ case for which there is a 5 % difference). This result gives strong indication that the dynamically computed α is the appropriate value, since it leads to a resolution-invariant value of the total wall stress. This finding may be particularly useful in the context of mesoscale atmospheric modelling, where typical horizontal spatial resolutions are comparable to the size of the entire horizontal domain considered here (e.g. several kilometres). It is also useful to recall that if one plots the mean velocity profiles as a function of $z/z_{0,G}$ (instead of as a function of

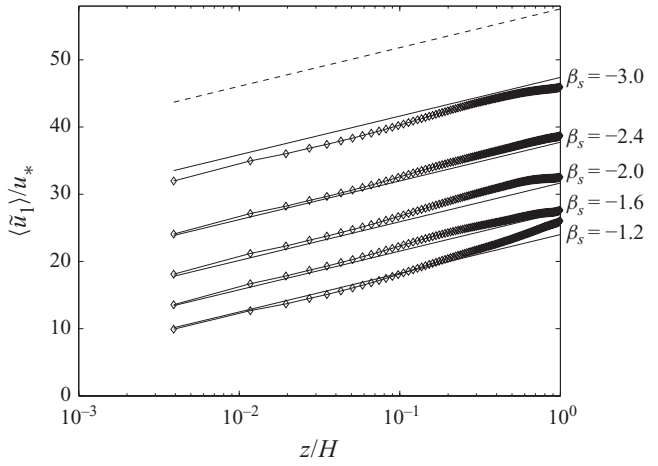

FIGURE 12. Non-dimensional mean streamwise velocity profiles for RFM surfaces with spectral slopes indicated on right of the figure. Symbols and lines: ◇, LES using $N = 128$; solid lines, logarithmic velocity profile $(1/\kappa)\log(z/z_{0,G})$, with $z_{0,G} = (z_{0,s}^2 + (\langle\alpha\rangle_t \sigma_G)^2)^{1/2}$ evaluated using the time average of the dynamically computed roughness parameter α; dashed line, logarithmic profile $(1/\kappa)\log(z/z_0)$ for $z_0 = z_{0,s}$.

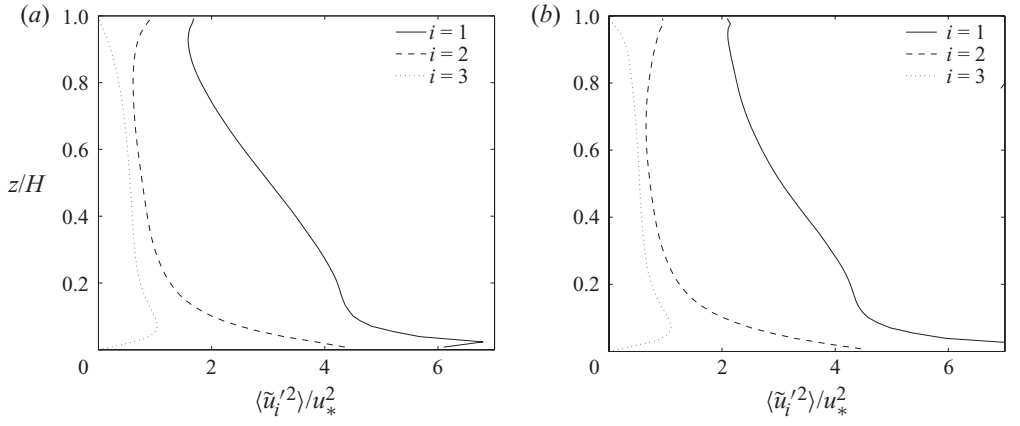

FIGURE 13. Vertical distribution of normalized velocity variances from $N = 64$ LES for surfaces with spectral exponent: (*a*) $\beta_s = -1.2$ and (*b*) $\beta_s = -3.0$. The variance quantity is denoted by the index in the legend.

z/H as done in figure 12), the results for the different surface roughnesses would all collapse closely into a single universal curve. This follows from the good agreement between LES and theoretical lines shown in figure 12, both in terms of the intercept (meaning good agreement with $z_{0,G}$) and the slope (meaning that the LES produces a value of $\kappa \sim 0.4$, the assumed theoretical value).

5.3. *Second-order moments*

Vertical profiles of variance and normalized shear stress are shown in figures 13 and 14, respectively. We show only results for the two spectral slopes, $\beta_s = -1.2$ and -3.0. Results for the surfaces with intermediate β_s values are very similar. The variance profiles are very similar to prior LES results reported for flow over rough surfaces, for example in Andrén *et al.* (2007), Porté-Agel *et al.* (2000) and

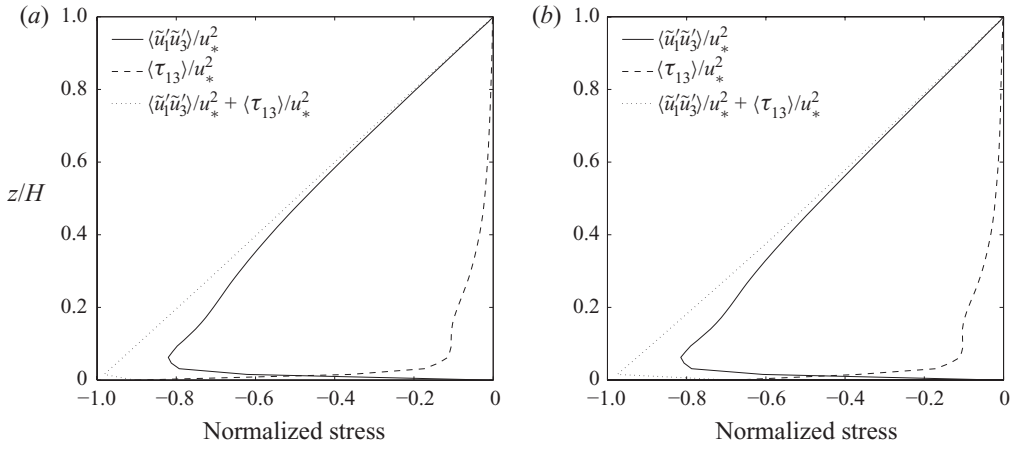

FIGURE 14. Vertical distribution of normalized shear stresses for the $N = 64$ case for surfaces with spectral exponent: (*a*) $\beta_s = -1.2$ and (*b*) $\beta_s = -3.0$. Shown are the resolved shear stress (solid line), the mean SGS shear stress (dashed) and their sum (dotted line).

Anderson, Basu & Letchford (2007). As can be seen, near the surface the streamwise variance increases slightly for the smoother surface, consistent with the expectation that a smoother surface damps the fluctuating motions to a smaller degree than a more rough surface. Still, the difference is small, which is not surprising considering that even though the spectral exponent varies among the surfaces, the unfiltered surface height variance is kept constant. The spanwise and wall-normal variances are essentially the same for both β_s values, except for some differences very near the wall. The shear stresses also show essentially no difference between very rough or very smooth surfaces. We conclude that there are very few effects of the surface spectral exponent on the variance profiles once these have been normalized with the friction velocity (or imposed pressure gradient). It is worth commenting on the fact that the normalized shear stress at the wall does not reach -1. This is due to the additional momentum loss associated with the resolved drag force represented by the SGD model, as discussed next.

The normalized stress results in figure 14 motivate a discussion of the total wall stress $-\langle\tau_{13}^T\rangle$ (5.1) at the surface, $z/H = 0$. Figure 15 shows the mean wall stress (5.1) for four of the surfaces with different spectral slopes, as a function of the LES resolution, expressed in terms of the horizontal resolution, Δ_x/H. First, we observe that in all cases the total wall stress is approximately equivalent to the total system forcing, as expected if the simulation is statistically stationary (top profile in each of the figures with data points indicated by crosses). Results demonstrate that the contribution from the SGS log law (○) and resolved surface-gradient (□) terms decrease and increase, respectively, as resolution is increased. Also, and as one may expect, we observe that the resolved surface-gradient component is greatest for the steepest spectral slope. Since the overall r.m.s. of the surface is fixed, increasing spectral slope reduces the fractional contribution from the SGS modes of the surface; increasing resolution (decreasing Δ) transfers dynamically important surface information from the SGS to resolved scale. These trends can be seen in figure 5. Still, it is remarkable that in all cases the largest contributor to the surface drag force is the SGS (log-law expression). The resolved part, while very important in the determination of the dynamic α, has a smaller contribution to the surface drag.

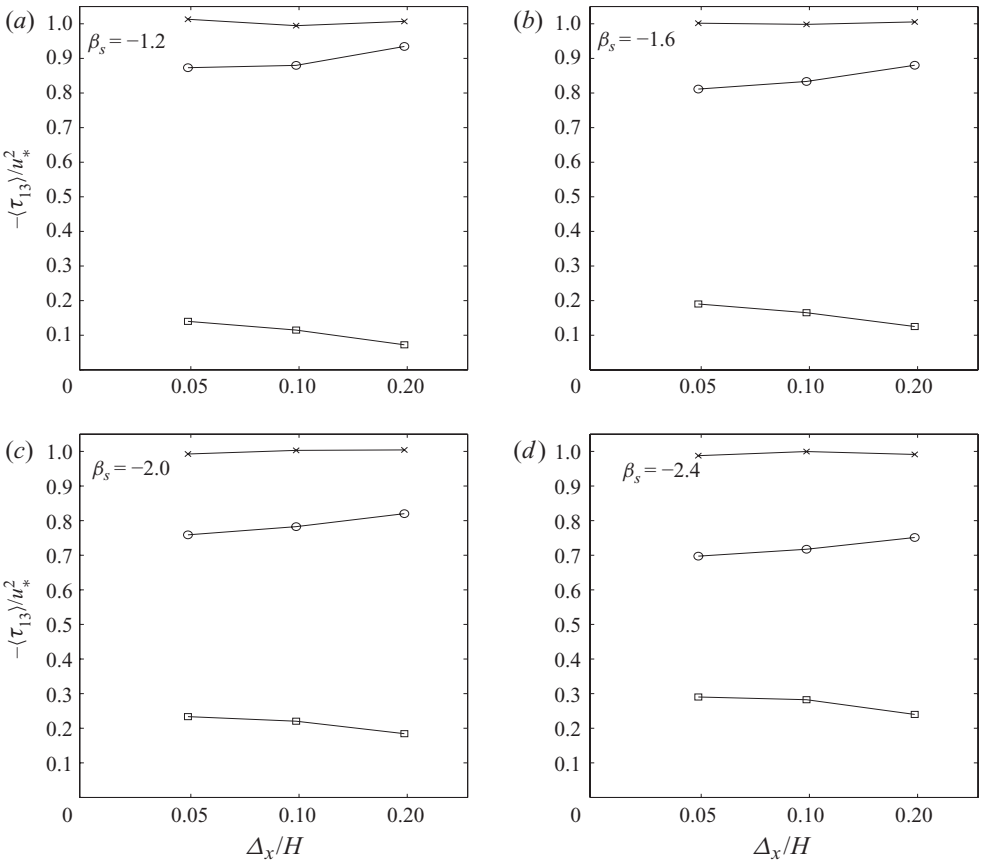

FIGURE 15. Plane-averaged total wall stress components at $z/H = 0$ for (*a*) $\beta_s = -1.2$, (*b*) $\beta_s = -1.6$, (*c*) $\beta_s = -2.0$ and (*d*) $\beta_s = -2.4$. Wall stress components shown correspond to ○, $\langle\tau_{13}^w\rangle$; □, $\langle f_1^{\Delta}\rangle\Delta_z$; ×, $\langle\tau_{13}^T\rangle$. The x-axis denotes horizontal grid resolution.

Another remarkable trend is the rapid decrease of α for the decreasing spectral exponent of the surface, as seen in figure 8. Recall that the overall variance of the surfaces is fixed. Therefore, making the surface smoother by varying the exponent β_s effectively reduces the slope of the surface. For power-law height spectra, the characteristic slope depends on resolution (since $\langle(\nabla h)^2\rangle \sim \int k^2 E_h \, \mathrm{d}k$ diverges at large wavenumbers for any $\beta \geqslant -1$). Therefore, it is not possible to meaningfully define a characteristic slope as was used e.g. in the work of Schultz & Flack (2009). Yet, in terms of trends, decreasing β_s decreases the surface slope. Our results of rapidly decreasing α and hydrodynamic roughness length for the smoother surfaces (with smaller surface slopes) are therefore qualitatively consistent with the results of Schultz & Flack (2009), who found the same trend for single-scale roughness elements (as long as the slope is smaller than ∼0.35).

6. Discussion and conclusions

A dynamic roughness model has been developed for high-Reynolds-number turbulent flows over multiscale, fractal-like surfaces with power-law height spectra; this problem is often encountered in geophysical flows. For representation in an

LES, the surfaces must be spatially filtered at the LES filter width. Drag effects associated with surface modes exceeding the filter width are here represented by an immersed boundary force that models the pressure drag using information from the topographic surface gradient $\nabla\tilde{h}$. Previously, Anderson & Meneveau (2010) tested this approach extensively for flows over a variety of horizontally resolved surfaces (i.e. that did not require non-trivial SGS contributions from unresolved roughness), finding favourable results. For the applications considered here, which include non-trivial SGS surface fluctuations below the filter width, an effective hydrodynamic roughness length is invoked in the context of local equilibrium log laws. The roughness length is parameterized through the product of height r.m.s. and an (initially unknown) roughness parameter α. Since the local r.m.s. varies spatially, the effective roughness length is spatially varying. The total wall stress is expressed through combination of the pressure drag and the log-law-based model, where the only unknown is the SGS roughness parameter, α. The parameter is evaluated under a self-consistency condition inspired by the Germano identity. It is applied to the plane-averaged total wall stress at two resolutions (grid- and test-filter width) and requires the total force to be independent of spatial resolution. Such exact self-consistency conditions provide valuable information to constrain models and/or evaluate parameters in computer simulations of multiscale flow processes.

The approach is tested systematically in LES of high-Reynolds-number flow over various rough, fractal-like surfaces. These surfaces have a wide range in height fluctuations and roughness, as characterized by the spectral exponent. In the absence of experimental or DNS validation data that can be readily compared with such cases at the appropriate resolutions, we opt to test the approach by means of LES at various resolutions. It is shown that if α is chosen incorrectly, simulating the same basic surface at varying resolutions yields different mean velocities, whereas if the dynamically obtained α is chosen, approximately resolution-independent results are obtained. The invariance to resolution shows that it is the correct result since one can imagine increasing the resolution further to ever smaller scales without changing the mean velocity. We remark that once the correct value of α has been determined, tests using this same value in a static implementation yield good results as well. The relative contributions of the resolved and SGS parts of the total wall stress display the expected trends with resolution and surface roughness.

Further applications of the dynamic roughness model to fluvial landscape surfaces obtained from digital elevation maps or from simulations of erosion processes (e.g. using the KPZ equation) will be reported elsewhere. Such more realistic natural landscapes are often not statistically isotropic. For instance, in fluvial landscapes, valleys and ridges can have preferred directions. The dynamic approach can also be expected to be applicable for such anisotropic surfaces, as long as the degree of anisotropy at resolved and subgrid scales is comparable. Further tests are needed to establish the applicability of the dynamic approach for anisotropic surfaces.

Besides assuming the validity of the equilibrium logarithmic scaling law, an important conceptual requirement for application of the DSR model is that the computational mesh grid- and test-filter must be applied in the landscape's 'self-similar' range, where the height statistics exhibit scale-invariant behaviour. As summarized in the Introduction, realistic landscapes are often characterized with power-law height spectra over a wide range of scales, which implies scale-invariance of the second-order statistical features of the surface. For applications where scale-invariance does not hold, one could envision further generalizations of the proposed dynamic approach. For instance, a scale-dependent version of the dynamic model can

be developed, in which α is allowed to depend on Δ according to some functionality that itself has parameters to be determined dynamically. As found in Porté-Agel *et al.* (2000) for the case of the Smagorinsky model in LES of turbulence, or in Passalacqua *et al.* (2006) for modelling unknown terms in KPZ simulations of eroding fluvial landscapes, scale-dependent implementation of the dynamic model involving filtering at additional scales (e.g. test–test–filtering, 4Δ) yields more accurate results. Furthermore, for spatially non-homogeneous surfaces (e.g. with patches of differing roughness), a more local implementation that does not average the wall stresses over the entire surface may be called for.

Applications of the approach may also be envisioned to determine roughness lengths for scalar fluxes such as potential temperature and humidity. Finally, the basic approach of assuming proportionality between the hydrodynamic roughness length and the r.m.s. of the SGS height is only one of many possibilities. As summarized in the Introduction, other expressions have been proposed to relate hydrodynamic roughness to geometric properties of the surface, such as including the average distance between dominant peaks. Other expressions based on peak–valley maxima, ten-point height (Bradshaw 2000), surface mean slope (Schultz & Flack 2009), surface skewness (Flack & Schultz 2010), etc. have also been proposed. The dynamic approach could also be applied to such expressions for determining unknown parameters which are inevitably necessary when relating hydrodynamic and geometric descriptions of roughness.

This work was supported by the National Science Foundation grants EAR 0609690 and AGS 1045189. Computational resources were provided by the Computational and Information Systems Laboratory at the National Center for Atmospheric Research. We thank Professors K. Flack and M. Schultz for valuable comments on the manuscript and Professors A. Nakayama, M. Chamecki, L. Shen, B. Kosovic and F. Porté-Agel for useful and stimulating comments on this work.

REFERENCES

Albertson, J. & Parlange, M. 1999 Surface length scales and shear stress: implications for land–atmosphere interaction over complex terrain. *Water Resour. Res.* **35**, 2121–2132.

Allen, J., Shockling, M., Kunkel, G. J. & Smits, A. J. 2007 Turbulent flow in smooth and rough pipes. *Phil. Trans. R. Soc. Lond.* A **365**, 699–714.

Allen, T. & Brown, A. R. 2002 Large-eddy simulation of turbulent-separated flow over rough hills. *Boundary-Layer Meteorol.* **102**, 177–198.

Anderson, W., Basu, S. & Letchford, C. W. 2007 Comparison of dynamic subgrid-scale models for simulations of neutrally buoyant shear-driven atmospheric boundary layer flows. *Environ. Fluid Mech.* **7**, 195–215.

Anderson, W. & Meneveau, C. 2010 A large-eddy simulation model for boundary layer flow over surfaces with horizontally resolved but vertically unresolved roughness elements. *Boundary-Layer Meteorol.* **137**, 397–415.

Andrén, A., Brown, A. R., Graf, J., Mason, P. J., Moeng, C.-H., Nieuwstadt, F. T. M. & Schumann, U. 1993 Large-eddy simulation of the neutrally stratified boundary layer: A comparison of four computer codes. *Q. J. R. Meteorol. Soc.* **120**, 1457–1484.

Avissar, R. & Pielke, R. A. 1989 A parameterization of heterogeneous land surfaces for atmospheric numerical models and its impact on regional meteorology. *Mon. Weath. Rev.* **114**, 2281–2296.

Bakken, O. M., Krogstad, P.-A., Ashrafian, A. & Andersson, H. 2005 Reynolds number effects in the outer layer of the turbulent flow in a channel with rough walls. *Phys. Fluids* **17**, 065101.

Bhaganagar, K. 2008 Direct numerical simulation of unsteady flow in channel with rough walls. *Phys. Fluids* **20**, 101508.

Bhaganagar, K., Kim, J. & Coleman, G. 2004 Effect of roughness on wall-bounded turbulence. *Flow Turbul. Combust.* **72**, 463–492.

Bou-Zeid, E., Meneveau, C. & Parlange, M. B. 2004 Large-eddy simulation of neutral atmospheric boundary layer flow over heterogeneous surfaces: blending height and effective roughness. *Water Resour. Res.* **40**, W02505.

Bou-Zeid, E., Meneveau, C. & Parlange, M. B. 2005 A scale-dependent Lagrangian dynamic model for large-eddy simulation of complex turbulent flows. *Phys. Fluids* **17**, 025105 (6–18).

Bou-Zeid, E., Parlange, M. B. & Meneveau, C. 2007 On the parameterization of surface roughness at regional scales. *J. Atmos. Sci.* **64**, 216–227.

Bradshaw, P. 2000 A note on 'critical roughness height' and 'transitional roughness'. *Phys. Fluids* **12**, 1611–1614.

Brown, A. R., Hobson, J. M. & Wood, N. 2001 Large-eddy simulation of neutral turbulent flow over rough sinusoidal ridges. *Boundary-Layer Meteorol.* **98**, 411–441.

Brutsaert, W. 2005 *Hydrology: An Introduction*. Cambridge University Press.

Castro, I. P. 2007 Rough-wall boundary layers: mean flow universality. *J. Fluid Mech.* **585**, 469–485

Castro, I. P., Cheng, H. & Reynolds, R. 2006 Turbulence over urban-type roughness: deductions from wind tunnel measurements. *Boundary-Layer Meteorol.* **118**, 109–131.

Chamecki, M., Meneveau, C. & Parlange, M. B. 2009 Large-eddy simulation of pollen transport in the atmospheric boundary layer. *J. Aerosol Sci.* **40**, 241–255.

Cheng, H. & Castro, I. P. 2002 Near-wall flow over urban-like roughness. *Boundary-Layer Meteorol.* **104**, 229–259.

Chester, S. & Meneveau, C. 2007 Renormalized numerical simulation of flow over planar and non-planar fractal trees. *Environ. Fluid Mech.* **7**, 195–215.

Chester, S., Meneveau, C. & Parlange, M. B. 2007 Modeling of turbulent flow over fractal trees with renormalized numerical simulation. *J. Comput. Phys.* **225**, 427–448.

Chow, F. K., Street, R. L., Xue, M. & Ferziger, J. H. 2000 Explicit filtering and reconstruction turbulence modeling for large-eddy simulation of neutral boundary layer flow. *J. Atmos. Sci.* **62**, 2058–2077.

Chow, F. T. & Street, R. L. 2009 Evaluation of turbulence closure models for large-eddy simulation over complex terrain: flow over Askervein Hill. *J. Appl. Meteorol. Climatol.* **48**, 1050–1065.

Coceal, O., Dobre, A., Thomas, T. G. & Belcher, S. E. 2007 Structure of turbulent flow over regular arrays of cubical roughness. *J. Fluid Mech.* **589**, 375–409.

Coceal, O., Thomas, T. G., Castro, I. P. & Belcher, S. E. 2006 Mean flow and turbulence statistics over groups of urban-like cubical obstacles. *Boundary-Layer Meteorol.* **121**, 491–519.

Colebrook, C. F. & White, C. M. 1937 Experiments with fluid friction in roughened pipes. *Proc. R. Soc. Lond.* A **161**, 367–381.

Deardorff, J. W. 1970 A numerical study of three-dimensional turbulent channel flow at large Reynolds numbers. *J. Fluid Mech.* **41**, 453–480.

Flack, K. A. & Schultz, M. P. 2010 Review of hydraulic roughness scales in the fully rough regime. *ASME J. Fluids Engng* **132**, 041203 (1–10).

Gal-Chen, T. & Sommerville, R. C. J. 1975*a* On the use of a coordinate transformation for the solution of the Navier–Stokes equations. *J. Comput. Phys.* **17**, 209–228.

Gal-Chen, T. & Sommerville, R. C. J. 1975*b* Numerical solution of the Navier–Stokes equations with topography. *J. Comput. Phys.* **17**, 276–310.

Garratt, J. R. 1977 *The Atmospheric Boundary Layer*. Cambridge University Press.

Germano, M. 1992 Turbulence: the filtering approach. *J. Fluid Mech.* **238**, 325–336.

Germano, M., Piomelli, U., Moin, P. & Cabot, W. H. 1991 A dynamic subgrid-scale eddy viscosity model. *Phys. Fluids* A **3**, 1760–1765.

Hobson, J. M., Wood, N. & Brown, A. R. 1999 Large-eddy simulations of neutrally stratified flow over surfaces with spatially varying roughness length. *Q. J. R. Meteorol. Soc.* **125**, 1937–1958.

Hurst, D. & Vassilicos, J. C. 2007 Scalings and decay of fractal-generated turbulence. *Phys. Fluids* **19**, 035103.

Iaccarino, G. & Verzicco, R. 2003 Immersed boundary technique for turbulent flow simulations. *Appl. Mech. Rev.* **56**, 331–347.

Jarvis, P. G., James, G. B. & Landsberg, J. J. 1976 Coniferous forest. In *Vegetation and the Atmosphere* (ed. J. L. Monteith), vol. 2, pp. 171–240. Academic Press.

Jiménez, J. 2004 Turbulent flow over rough walls. *Annu. Rev. Fluid Mech.* **36**, 173–196.

Kaimal, J. C. & Finnigan, J. J. 1994 *Atmospheric Boundary Layer Flows: Their Structure and Measurement*. Oxford University Press.

Kanda, M., Moriwaki, R. & Kasamatsu, F. 2004 Large-eddy simulation of turbulent organized structures within and above explicitly resolved cube arrays. *Boundary-Layer Meteorol.* **112**, 343–368.

Kosović, B. 1997 Subgrid-scale modelling for the large-eddy simulation of high-Reynolds-number boundary layers. *J. Fluid Mech.* **336**, 151–182.

Lilly, D. K. 1966 On the application of the eddy viscosity concept in the inertial subrange of turbulence. *NCAR Manuscript* **123**, 1–19.

Mandelbrot, B. B. 1982 *The Fractal Geometry of Nature*. Freeman.

Mason, P. J. & Callen, N. S. 1986 On the magnitude of the subgrid-scale eddy coefficient in large-eddy simulations of turbulent channel flow. *J. Fluid Mech.* **162**, 439–462.

Mavriplis, D. J. 1997 Unstructured grid techniques. *Annu. Rev. Fluid Mech.* **29**, 473–514.

Meneveau, C. & Katz, J. 2000 Scale-invariance and turbulence models for large-eddy simulation. *Annu. Rev. Fluid Mech.* **32**, 1–32.

Mittal, R. & Iaccarino, G. 2005 Immersed boundary methods. *Annu. Rev. Fluid Mech.* **37**, 239–261

Monin, A. S. & Obukhov, A. M. 1954 Basic laws of turbulent mixing in the ground layer of the atmosphere. *Tr. Geofiz. Inst., Akad. Nauk SSSR* **151**, 163–187.

Nakayama, A., Hori, K. & Street, R. L. 2004 Filtering and LES of flow over irregular rough boundary. *Center for Turbulence Res.: Proc. of Summer Prog.* 145–156.

Nakayama, A. & Sakio, K. 2002 Simulation of flows over wavy rough boundaries. *Center for Turbulence Res., Annu. Res. Briefs, Stanford Univ./NASA Ames Res. Center* 313–324.

Nikuradse, J. 1950 Laws of flow in rough pipes. *NACA TM* 1292.

Orey S. 1970 *Z. Wahrscheinlichkeitstheorie Verw. Geb.* **15**, 249.

Orlandi, P. & Leonardi, S. 2006 Direct numerical simulation of channel flow with a rib-roughened wall. *J. Turbul.* **7** (53), 1–22.

Orlandi, P. & Leonardi, S. 2008 Direct numerical simulation of three-dimensional turbulent rough channels: parameterization and flow physics. *J. Fluid Mech.* **606**, 399–415.

Orszag, S. A. 1970 Transform method for calculation of vector coupled sums: Application to the spectral form of the vorticity equation. *J. Atmos. Sci.* **27**, 890–895.

Passalacqua, P., Porté-Agel, F., Foufoula-Georgiou, E. & Paola, C. 2006 Application of dynamic subgrid-scale concepts from large-eddy simulations to modeling landscape evolution. *Water Resour. Res.* **42**, W06D11.

Phillips, O. M. 1958 The equilibrium range in the spectrum of wind-generated waves. *J. Fluid Mech.* **4**, 426–434.

Piomelli, U., Moin, P. & Ferziger, J. H. 1988 Model consistency in large eddy simulation of turbulent channel flows. *Phys. Fluids* **31**, 1884–1891.

Porté-Agel, F., Meneveau, C. & Parlange, M. B. 2000 A scale-dependent dynamic model for large-eddy simulation: application to a neutral atmospheric boundary layer. *J. Fluid Mech.* **415**, 261–284.

Queiros-Conde, D. & Vassilicos, J. C. 2001 Turbulent wakes of 3D fractal grids. In *Intermittency in Turbulent Flows* (ed. J. C. Vassilicos), pp. 136–166. Cambridge University Press.

Raupach, M. R. 1994 Simplified expressions for vegetation roughness length and zero-plane displacement as functions of canopy height and area index. *Boundary-Layer Meteorol.* **71**, 211–216.

Raupach, M. R., Antonia, R. A. & Rajagopalan, S. 1991 Rough-wall turbulent boundary layers. *Appl. Mech. Rev.* **44**, 1–25.

Rodriguez-Iturbe, I., Marani, M., Rigon, R. & Rinaldo, A. 1994 Self-organized river basin landscapes: Fractal and multifractal characteristics. *Water Resour. Res.* **30**, 3531–3539.

Rodriguez-Iturbe, I. & Rinaldo, A. 1997 *Fractal River Basins: Chance and Self-Organization*. Cambridge University Press.

Schlichting, H. 1936 Experimentelle Untersuchungen zum Rauhigkeitsproblem. *Ing.-Arch.* **7**, 1–34.

Schultz, M. P. & Flack, K. A. 2005 Outer layer similarity in fully rough turbulent boundary layers. *Exp. Fluids* **38**, 328–340.

Schultz, M. P. & Flack, K. A. 2007 The rough-wall turbulent boundary layer from the hydraulically smooth to the fully rough. *J. Fluid Mech.* **580**, 381–405.

Schultz, M. P. & Flack, K. A. 2009 Turbulent boundary layers on a systematically-varied rough wall. *Phys. Fluids* **21**, 015104.

Seoud, R. E. & Vassilicos, J. C. 2007 Dissipation and decay of fractal-generated turbulence. *Phys. Fluids* **19**, 105108.

Shaw, R. H. & Schumann, U. 1992 Large-eddy simulation of turbulent flow above and within a forest. *Boundary-Layer. Meteorol.* **61**, 47–64.

Shockling, M. A., Allen, J. J. & Smits, A. J. 2006 Roughness effects in turbulent pipe flow. *J. Fluid Mech.* **564**, 267–285.

Smagorinsky, J. 1963 General circulation experiments with the primitive equations, Part 1. The basic experiment. *Mon. Weath. Rev.* **91**, 99–164.

Smith, F. B. & Carson, D. J. 1977 Some thoughts on the specification of the boundary-layer relevant to numerical modelling. *Boundary-Layer. Meteorol.* **12**, 307–330.

Staicu, A., Mazzi, B., Vassilicos, J. C. & van der Water, W. 2003 Turbulent wakes of fractal objects. *Phys. Rev.* E **67**, 066306.

Tsai, J.-L. & Tsuang, B.-J. 2005 Aerodynamic roughness over an urban area and over two farmlands in a populated area as determined by wind profiles and surface energy flux measurements. *Agric. Forest. Meteorol.* **132**, 154–170.

Wan, F. & Porté-Agel, F. 2010 A large-eddy simulation study of turbulent flow over multiscale topography. *EGU Gen. Assembly,* vol. 12, EGU2010-10875.

Xie, Z. T., Coceal, O. & Castro, I. P. 2008 Large-eddy simulation of flows over random urban-like obstacles. *Boundary-Layer Meteorol.* **129**, 1–23.

Zagarola, M. V. & Smits, A. J. 1998 Mean-flow scaling of turbulent pipe flow. *J. Fluid Mech.* **373**, 33–79.